UV-Visible photo-reactivity of permanently polarized inorganic nanotubes coupled to gold nanoparticles

Sabyasachi Patra, Fabienne Testard, Frédéric Gobeaux, Lorette Sicard, Delphine Shaming, Sophie Le Caër, Antoine Thill

UV-Visible photo-reactivity of permanently polarized inorganic nanotubes coupled to gold nanoparticles

Sabyasachi Patra[a,b,*], Fabienne Testard[a], Frédéric Gobeaux[a], Lorette Sicard[c], Delphine Shaming[c], Sophie Le Caër[a,*], Antoine Thill[a,*]

[a]Université Paris-Saclay, CEA, CNRS, NIMBE, 91191, Gif-sur-Yvette, France

[b]Radiochemistry Division, Bhabha Atomic Research Centre, Trombay, Mumbai - 400085, India

[c]Université de Paris, ITODYS, CNRS, UMR 7086, 15 rue J.-A. deBaïf, F-75013, Paris, France

*E-mail: spatra@barc.gov.in, sspatra86@gmail.com, sophie.le-caer@cea.fr, antoine.thill@cea.fr

Abstract

Hybrid aluminosilicate nanotubes (Imo-CH_3) have the ability to trap small organic molecules inside their hydrophobic internal cavity while being dispersed in water owing to their hydrophilic external surface. They also display a curvature-induced polarization of their wall, which favors reduction outside the nanotubes and oxidation inside. Here, we coupled bare plasmonic gold nanoparticles (GNP) with Imo-CH_3 and analyzed for the first time the redox reactivity of these hybrid nano-reactors upon UV illumination. We show that the coupling between GNPs and Imo-CH_3 significantly enhances the nanotube photocatalytic activity, with a large part of water reduction occurring directly on the gold surface. The coupling mechanism strongly influences the initial H_2 production rate, which can go from ×10 to more than ×90 as compared to bare Imo-CH_3 depending on the synthesis route of the GNPs. The present results show that this hybrid photocatalytic nano-reactor benefits from a synergy of polarization and confinement effects that facilitate efficient H_2 production.

Keywords: photo-catalysis; nanoconfinement; metal-semiconductor coupling; water reduction; energy production

1. Introduction

Considering the combined threat of global warming and increasing energy demand, harvesting energy from the sun with well-balanced, economical and environmentally-friendly processes that produce fuel or chemicals is necessary.[1-5] Trialing original semiconductor structures as photocatalysts to help circumvent the well-known limitations of such energy harvesting is a potentially rewarding strategy that has been intensively explored.[6-12] In this context, aluminosilicate nanotubes (NTs), commonly known as imogolites with a general formula of $(OH)_3Al_2O_3Si(OH)$ (Imo-OH), can be considered as potential (co)photocatalysts.

Imogolite NTs naturally possess a hydrophilic cavity and have an external diameter of 2.5 nm, an internal diameter of 1.5 nm and a length of up to several microns. Imogolite NTs can also be prepared with a hydrophobic methyl-functionalized internal surface to form hybrid imogolites (Imo-CH_3).[13] For both types of NTs, density functional theory (DFT) computations have predicted the physical separation of valence and conduction bands and the existence of a permanent polarization of the NT wall, thus offering potential co-photocatalytic properties.[14-17] The presence of intra-wall polarization in Imo-CH_3 NTs has been qualitatively demonstrated by our group thanks to solvatochromic dye, Nile Red, and by following the change of its optical response upon encapsulation inside the Imo-CH_3 cavity.[18] We have recently demonstrated and quantified this curvature-induced polarization in both Imo-OH and in Imo-CH_3 NTs.[19,20] We have

also experimentally shown that, upon excitation, electrons with sufficient energy are driven outside the NTs, while holes are driven inside.[19] The potential of Imo-CH_3 as a photocatalytic nano-reactor was then highlighted through the photodegradation of dibenzo(a,h)anthracene (DBAN), a phototoxic polycyclic aromatic hydrocarbon molecule chosen as a model pollutant.[21] We showed that DBAN is efficiently confined in the internal cavity of Imo-CH_3 NTs and that the UV degradation of confined DBAN is significantly enhanced. Indeed, the permanent polarization aids charge separation by preventing the recombination of electrons and holes formed upon illumination and by separating photo-induced redox reactions on different surfaces (the inner and outer surfaces for oxidative and reductive reactions, respectively). The partitioning of redox reactions on different surfaces was even suspected to induce, on the external surface, a partial reduction of $\mathbf{CO_2}$ produced by the internal mineralization of DBAN.

At the same time, coupling semiconductors with plasmonic metal nanoparticles as co-catalyst has been shown to significantly enhance their photocatalytic efficiency.[21,22] Some of the mechanisms of these enhancements are known. For example, under UV light, metal nanoparticles can act as an electron reservoir. Conversely, under visible light, they can inject energetic electrons produced by the relaxation of the nanoparticle plasmon into the semiconductor.[24-30] Yang *et al.* have reviewed the roles of noble metal co-catalysts for water reduction reaction on a semiconductor photocatalyst.[31] They have highlighted the fact that, in spite of having the required thermodynamic potential for water splitting reaction, the photogenerated charged pairs (electrons and holes) may undergo facile recombination in absence of suitable reaction sites on the surface of the light harvesting semiconductor, even in the presence of sacrificial hole scavengers, and cannot show a reasonable photocatalytic activity for H_2 production without a co-catalyst. Noble metal co-catalysts coupled with the light harvesting semiconductor can facilitate the course of a

photocatalytic reaction by serving as the active reaction sites and by reducing the recombination probability through facilitated charge separation and transport across the noble metal-semiconductor junctions/interfaces. In addition to their role as electron sinks, noble metal co-catalysts can also provide efficient proton reduction sites, thereby facilitating the H_2 production.[31] Natural imogolite (Imo-OH) has previously been coupled to metal nanoparticles as shown by Liz-Marzan and Philipse,[32,33] who demonstrated the formation of highly stable hydrosols of platinum, gold, silver and many bimetallic systems immobilized on Imo-OH fibers by chemical reduction route ($NaBH_4$ being the reductant) and without the need of any external stabilizing polymer. They have confirmed that, due to the large surface area, imogolite nanotubes have multiple adhesion sites on external surface and that the adsorption interactions of metal nanoparticles on such sites are irreversible. This imparts an excellent stability to the coupled metal nanoparticles by preventing self-aggregation on the surface. They have attributed this strong interaction between the metal nanoparticles and imogolite surface as combined Van der Waals and electrostatic attractions where the adsorption of metal nanoparticles to a neighbouring nanotube is hindered by the formation of the electrical double layer. However, the formation of metal nanoparticles on the surface of more versatile hybrid imogolite (Imo-CH_3) NTs, as well as the induced photo-reactivity upon illumination, has not been described yet. The aim of the present work is to bridge this gap.

In this article, we explore the enhancement of the photocatalytic properties of methyl imogolite (Imo-CH_3) by gold nanoparticles (GNPs). Two strategies to couple the NTs and GNPs were investigated. GNPs were synthesized on the external surface of Imo-CH_3 by a deposition-precipitation mechanism followed by either a photolytic or radiolytic reduction step. The complete characterization of the materials obtained by both methods (UV photolysis and gamma

radiolysis) was then performed using various techniques including SAXS, TEM, XPS and UV-Vis prior to the characterization of their photocatalytic reactivity. We show here that the presence of GNPs on imogolite significantly enhances its photocatalytic dihydrogen production compared to pristine imogolite. Further, the synthesis route of the GNP-coupled Imo-CH_3 had a clear impact on its catalytic efficiency. These results are discussed, and the roles of particle size and the chemical species present on the external surface of the NTs are highlighted.

2. Experimental Section

2.1. Materials

Aluminum-tri-sec-butoxide (97%), trimethoxymethylsilane (TMMS, 98%), potassium bromide (FT-IR grade, ≥ 99%), hydrochloric acid (HCl, 37%), chloroauric acid ($HAuCl_4$, $3H_2O$, ≥99.9% trace metals basis) and sodium hydroxide (NaOH, ≥ 98%) were purchased from Sigma-Aldrich and used without further purification. Ultra-high purity Ar (99.9999%) purchased from Air Products was used for the degassing of solutions. MilliQ water with a conductivity of 18.2 MΩ.cm at 25 ^{o}C was used throughout the present study.

2.2. Synthesis of Imo-CH_3 nanotubes

Methyl-functionalized imogolite NTs (Imo-CH_3) were synthesized following a procedure inspired by Bottero *et al.*[13] In brief, aluminum-tri-*sec*-butoxide was dissolved in a hydrochloric acid solution (75 mM) and trimethoxymethylsilane was added dropwise under stirring until the Si/Al molar ratio reached 0.6. The mixture was then vigorously stirred at ambient temperature for an hour and subsequently placed in an oven at 90 ^{o}C for 5 days. A slightly turbid solution was then obtained which showed birefringence under cross-polarized light, indicating the formation of imogolite NTs. The resultant nanotube solution was dialyzed against MilliQ water using a

membrane with molecular weight cutoffs of 6-8 kDa to remove alcohols and excess salt. The NT concentration in the dialyzed solution was obtained by measuring the mass of solid after drying a known volume of Imo-CH_3 solution in an oven at 45 ^{o}C. The concentration of the aqueous Imo-CH_3 suspension was found to be 8.4 g.L^{-1}. If required, this suspension was diluted with MilliQ water in order to obtain a lower concentration.

2.3. Synthesis of gold nanoparticles on the external surface of Imo-CH_3 nanotubes

$HAuCl_4$ stock solution at a concentration of 1 mg.mL^{-1} was prepared and stored in the dark at 4 °C. A known volume of the Imo-CH_3 solution (concentration of 8.4 mg.mL^{-1}) was mixed with a known volume of the $HAuCl_4$ stock solution and the pH of the mixture solution was brought to 8 by the dropwise addition of a 1M NaOH solution. After pH adjustment, the solution turned from light yellow to colorless with a slight turbidity. Subsequently, the solution was heated at 80°C for 1 hour under stirring in dark. The solution was dialyzed against MilliQ water using a 6-8 kDa membrane to remove the unreacted salts. Subsequently, this dialyzed solution will be denoted as *Solution-A*, which was used as the precursor solution for the additional reduction steps performed either by photolysis or radiolysis to obtain gold nanoparticles coupled to the external surface of Imo-CH_3 NTs. Propan-2-ol was added (10 vol%) to *Solution-A* prior to photolysis/radiolysis.

Photolysis was performed in a standard quartz cuvette under air atmosphere using a benchtop UV illumination chamber consisting of eight 15 W low pressure mercury lamps (OSRAM G15T8/OF, ozone free) emitting at 254 nm, with an incident photon intensity of 6.9 x 10^{-5} Einstein.L^{-1}.s^{-1} (equivalent to 4.15 × 10^{19} photons.L^{-1}.s^{-1}) measured by a potassium ferrioxalate actinometer solution.[32]

Radiolysis was performed using a Gammacell 3000 containing a ^{137}Cs source. The experiments were performed under argon atmosphere, as no reduction of gold was observed under air atmosphere. The dose rate (4.9 ± 0.7 Gy min^{-1}, with 1 Gy = 1 J kg^{-1}) was determined using a Fricke dosimeter.[35] Radiolysis of *Solution-A* was done in a Pyrex glass ampoule, pre-bubbled with argon for 30 min to remove the dissolved oxygen. This was followed by five cycles of degassing at 5 x 10^{-3} mbar/filling with 1.5 bar of argon, ensuring a very clean final argon atmosphere in the ampoules.

After illumination or irradiation, the color of the *Solution-A* turned to intense red, characteristic of GNPs. It was then further dialyzed against MilliQ water to remove excess propan-2-ol.

2.4. Characterization of Imo-CH_3 and gold nanoparticle-coupled Imo-CH_3 NTs

2.4.1. UV-Vis and fluorescence spectroscopy

GNPs in the presence of Imo-CH_3 NTs during photolysis/radiolysis processes were characterized by UV-Vis spectroscopy using a UB-2450 Shimadzu spectrophotometer. Spectra were acquired in the 400-700 nm wavelength range. Fluorescence emission spectra of pristine Imo-CH_3 and GNP-coupled Imo-CH_3 NTs were acquired using a HORIBA Fluoromax-4 spectrofluorometer. Emission spectra were measured in the 240-800 nm wavelength range, and excitation was performed in the 200-220 nm range.

2.4.2. Small angle-X-ray scattering

Small angle X-ray scattering (SAXS) experiments were performed for pristine Imo-CH_3 NTs and GNP-coupled Imo-CH_3 NTs in aqueous suspension (sealed in glass capillaries with a diameter of 1.6 mm) using two laboratory X-ray instruments (a XEUSS 2.0 from Xenocs and a custom

system named ChemSAXS, described below) at the SWAXS Laboratory of University Paris-Saclay.

For the XEUSS 2.0 set-up, the X-ray beam was produced by a copper microfocus X-ray source (8 keV, GeniX^{3D}, Xenocs), and scattered X-rays were detected by a Pilatus 1M detector (Dectris). The q range from 0.029 to 1.37 Å^{-1} was studied using a sample-to-detector distance of 44.7 cm and calibrated with a AgBe standard. The counting time was 1.5 hours for each measurement.

For the ChemSAXS set-up, the X-ray beam was produced by a copper source (8 keV, GeniX^{3D}, Xenocs), and scattered X-rays were detected by a Pilatus 200K detector (Dectris). The q range from 0.008 to 0.35 Å^{-1} was studied using a sample-to-detector distance of 112.5 cm and calibrated with a AgBe standard. The counting time was 1 hour for each measurement.

For both platforms, the detector count was normalized to the differential cross sections per volume from the direct beam measurement. Data treatment (radial averaging and correction of scattering contribution of water, empty glass capillary and electronic background) was performed using an in-house extension of the open-source Python SAXS software (pySAXS)[36,37] to extract the absolute intensity $I(q)$ vs. the scattering vector (q), where $q = 4\pi\sin\theta/\lambda$ (λ and 2θ denoting the incident wavelength and the scattering angle, respectively). Adjustment of the SAXS patterns was obtained with the pySAXS software.

2.4.3. Inductively coupled plasma mass spectrometry (ICP-MS)

The gold loading on the GNP-coupled Imo-CH_3 samples was characterized by ICP-MS (ICMPS ICAPQ Quadrupole model, ThermoFisher Scientific). The elements studied were gold and silicon. A known mass of GNP-coupled Imo-CH_3 samples was dissolved in aqua regia and further

diluted in MilliQ water before ICP-MS analysis. The concentration of silicon was used to calculate the amount of gold relative to the amount of Imo-CH_3.

2.4.4. X-ray photoelectron spectroscopy (XPS)

X-ray photoelectron spectroscopy (XPS) measurements of the Imo-CH_3 solution containing gold(III) ions (i.e., *Solution-A*) and GNP-coupled Imo-CH_3 NTs were carried out using a ThermoVGESCALAB 250 system equipped with a micro-focused, monochromatic Al Kα X-ray source (1486.6 eV) and a magnetic lens, which increases the electron acceptance angle and, hence, the sensitivity. The X-ray spot size was 650 μm (15 kV, 150 W). The samples were prepared by depositing several drops of the imogolite aqueous suspension on an indium tin oxide (ITO) substrate. The spectra were acquired in the constant analyzer energy mode with pass energies of 150.0 and 15.0 eV for the general survey and the narrow scans, respectively with a step size for core level spectra of 0.1 eV. The binding energy peak positions were calibrated by setting the C1s component of adventitious carbon at 285.0 eV. The Avantage software was used for data acquisition and processing. The Au 4f contributions were fitted considering, for each Au species, the two contributions of Au $4f_{7/2}$ and Au $4f_{5/2}$ with an energy difference close to 3.7 eV and a relative intensity of 4:3.[38]

2.4.5. Transmission and scanning electron microscopy (TEM/SEM)

Electron microscopy was performed for the pristine and the GNP-coupled Imo-CH_3 NTs. Both transmission and scanning electron microscopy (TEM and SEM) analyses were performed. TEM observations were made using both conventional and cryogenic transmission electron microscopes. Sample preparation for conventional TEM consisted of the deposition of a 5 μL drop of the aqueous sample on a carbon-coated copper grid and the subsequent blotting of excess

liquid with filter paper. A Philips CM12 electron microscope at an operating voltage of 80 kV was used. Cryo-TEM samples were prepared by using a fully-automated Vitrobot System (FEI Company). Briefly, a 5 μL drop of the aqueous sample was deposited on a plasma pre-treated electron microscopy grid covered with holey carbon film (Quantifoil R2/2). After removing the excess liquid with filter paper, the grid was rapidly dipped in liquid ethane to form a thin film of vitreous ice. The cryo-TEM observations were carried out at -180 ^{o}C using a JEOL 2010 FEG microscope working at 200 kV. A Gatan camera was used to capture images during both the conventional and cryo-TEM observations.

Field emission scanning electron microscopy images were obtained with a Zeiss SUPRA 40 FESEM. The samples were prepared by drying a drop of an aqueous sample on a Si substrate.

2.5. Photocatalytic water reduction reaction

GNP-coupled Imo-CH_3 NTs produced by either UV photolysis or gamma radiolysis were tested as nanoreactors for the photocatalytic reduction of water. Photocatalytic experiments were conducted under two different conditions: (i) under a monochromatic UV light source of 254 nm (incident photon intensity of 6.9×10^{-5} Einstein.L^{-1}.s^{-1}), previously used for nanoparticle synthesis; and (ii) under the broad visible light from a solar simulator (111.3 Einstein.L^{-1}.s^{-1} at 480 nm). The photocatalytic water reduction under UV light was conducted in a modified Pyrex glass ampoule with a standard quartz cuvette (1 cm path length) at the bottom, whereas the reactions under visible light were performed in a standard Pyrex glass ampoule, which prevents UV light penetration.

For both illuminations, the pre-treatment of the suspension was similar. The aqueous suspension of pristine Imo-CH_3 or of GNP-coupled Imo-$CH_3$was mixed with 20 vol% propan-2-ol, used as a

sacrificial hole scavenger, and placed in the ampoule (total solution volume of 2 mL). The solution was then pre-bubbled with argon for 30 min to remove dissolved oxygen. This was then followed by five cycles of degassing at 5 x 10^{-3} mbar/filling with 1.5 bars of argon. The samples were then illuminated with UV or visible light. H_2, CH_4, CO and CO_2 gases were then identified and, if present, quantified by micro-gas chromatography (μ-GC-R3000, SRA instrument) using ultra-high purity helium and argon as carrier gases.

3. Results and Discussion

The synthesized Imo-CH_3 NTs were characterized after dialysis by Cryo-TEM (Figure S1, Electronic Supplementary Information). Single-walled Imo-CH_3 nanotubes were found to be mostly present in small bundles of a few tubes, rather than as isolated tubes. A typical SAXS signature of the Imo-CH_3 suspension (at 8.4 g.L^{-1}) is shown in Figure 1 (black circles). The well-defined oscillations of the SAXS profile of imogolite suspensions are due to the monodisperse radius of the Imo-CH_3 NTs. The adjustment of the experimental SAXS intensity with a core-shell cylinder model enabled determining an outer diameter of ~ 3 nm.[39] The shell of pristine Imo-CH_3 is composed of rings containing 16 $(OH)_3Al_2O_3SiOCH_3$ units (see Figure S2 and Table S1 in Electronic Supplementary Information). The slight deformation of the oscillations and the intensity in the lower *q*-range confirms the formation of small bundles even in solution.

3.1. Anchoring gold(III) ions on the external surface of Imo-CH_3 NTs

Due to the reasonably high value of the zero point charge of imogolite NTs (PZC = 10),[40-42] gold(III) ions could be anchored on their external surface by the deposition-precipitation of gold metal salts under alkaline conditions (pH = 8), following a slightly modified version of the protocol described by Haruta.[43,44] At pH 8, the fully hydrolysed $Au(OH_4)^-$ ions predominates and

can form complexes to form Al-O-Au$(OH)_2$ type of links on the external surface of Imo-CH_3 NTs. The obtained solution named "*Solution-A*" (see section 2.3 in Experimental Section) was analyzed by SAXS (Figure 1, orange triangles). The presence of gold in *Solution-A* after dialysis was evidenced by an increased intensity in the low *q*-range on the SAXS pattern as compared to pristine imogolite, and by a slight modification of the typical imogolite oscillation signature at higher *q*-range. After subtraction of the imogolite/water suspension SAXS intensity, the residual intensity can be interpreted as the signature of gold(III) ions localized around imogolite NTs. Figure 1 illustrates the adjustment of this signal by a fractal organization of core-shell cylinders model with the presence of gold dispersed as an outer layer (the "shell") around imogolite (the "core") (see Section 3 in Electronic Supplementary Information). The scattering length density (SLD) of the shell is calculated by taking into account all the electrons of the Au atoms and the associated initial chloride ions, using the Au(III) composition determined by ICP-MS (8.5% w/w of gold per Imo-CH_3 NT). At pH = 8, most of the chloride ions from $AuCl_4^-$ should be replaced by OH^- ions. However, due to high affinity of the positively-charged imogolite external surface towards Cl^- anions by means of outer sphere complexation,[45] it is reasonable to hypothesize that the exchanged Cl^- ions will still be present on the imogolite surface as adsorbed anions (the presence of Cl^- is confirmed by XPS, see Figure S3, Electronic Supplementary Information). Therefore, they will also contribute to the SAXS signal of the shell. The size of the internal diameter of the gold shell is fixed by the external diameter of imogolite (3 nm). The concentration of imogolite is fixed by the weight composition of the sample (2.3 $mg.mL^{-1}$). The thickness of the shell of the SAXS model was then adjusted to 0.67 nm in order to fit the experimental SAXS pattern. Table S2 summarizes the parameters used for the adjustment of the SAXS data. *Solution-A* was then subjected either to photolysis under UV light (253.7 nm) or to gamma radiolysis to form GNPs.

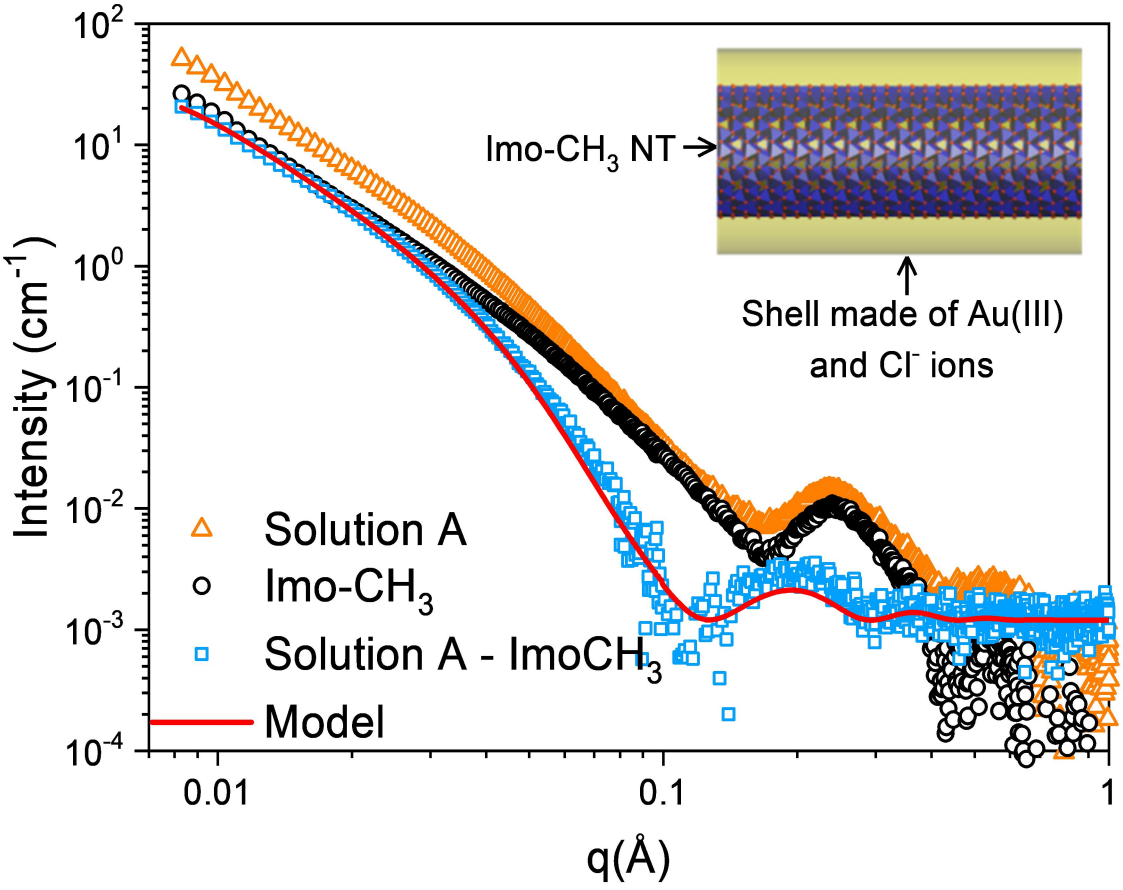

Figure 1. *SAXS profile of Solution-A (orange triangles), pristine imogolite (black circles) and Solution-A after subtraction of pristine Imo-CH$_3$ scattering contribution (blue squares). The simulated SAXS profile for hollow cylinders made of surface adsorbed Au(III) and Cl$^-$ ions plus their fractal organization is also shown (red line curve) (see SI for details).*

3.2. Formation of gold nanoparticles on the external surface of Imo-CH$_3$ NTs

3.2.1. UV-photolysis of Solution-A

UV illumination of *Solution-A* in the presence of propan-2-ol (10% per volume) turned the color of the solution to intense red, characteristic of plasmonic GNPs (Figure 2, top). Indeed,

the photocatalytic role of imogolite NTs in forming GNPs was confirmed by a control experiment (see Section 5, Figure S4 in Electronic Supplementary Information). In order to obtain the size distribution of these GNPs with reasonable statistics, the photo-reduced solution was subjected to both conventional SEM and TEM analysis. Figure 2a,b shows the SEM and Figure 2c,d the TEM images of Imo-CH_3 with GNPs. Clearly, a large number of GNPs were attached to the Imo-CH_3 NTs. Figure 2e,f shows the cryo-TEM image of the photo-reduced solution (after dialysis), evidencing the formation of spherical gold NPs attached to the wall of Imo-CH_3 NTs. Additionally, the tubular morphology of the single-walled Imo-CH_3 NTs remained intact after the GNP attachment. Figure 2g shows the SAXS profile of the photolytically-produced GNP-coupled Imo-CH_3 nanotubes after subtraction of the pristine Imo-CH_3 scattering contribution (black circles) together with the simulated SAXS profile of a fractal aggregate of a Gaussian polydispersed spherical particle model (red solid line). In the low *q*-range, a typical signal from the mass fractal organization of gold NPs and small clusters or smaller gold nanoparticles adsorbed on imogolite are visible. Table S3 in the Electronic Supplementary Information summarizes the parameters used for the model. The size of the GNPs as obtained from SAXS analysis (9.5 ± 2.0 nm) is in agreement with the TEM/SEM analysis (10 nm) (Figure 2h). Moreover, the UV-Vis spectra of *Solution-A* under UV illumination (Figure 2i) show a continuous rise of the Localized Surface Plasmon Resonance (LSPR) band at ~525 nm, indicating the formation of plasmonic GNPs (Figure 2i). However, the number of particles as obtained by SAXS (10^{13} spheres.cm^{-3} considering spherical particles) gives a lower volume fraction of gold (5.1×10^{-6}) than expected from the ICP-MS measurement (9.1×10^{-6}). This latter measurement leads to 8.2 ± 0.1 $\%_{w/w}$ of gold attached to Imo-CH_3 NTs, which is consistent with the targeted concentration of 8.5 wt%. The difference between the SAXS and the ICP-MS values could be attributed to a significant proportion (~44$\%_{v/v}$) of gold still present as nearly atomic size

or organized into clusters (below 1 nm) all over the surface of the Imo-CH_3 NTs. This contribution has too low of a scattering signature in the high q range to be detectable by SAXS.

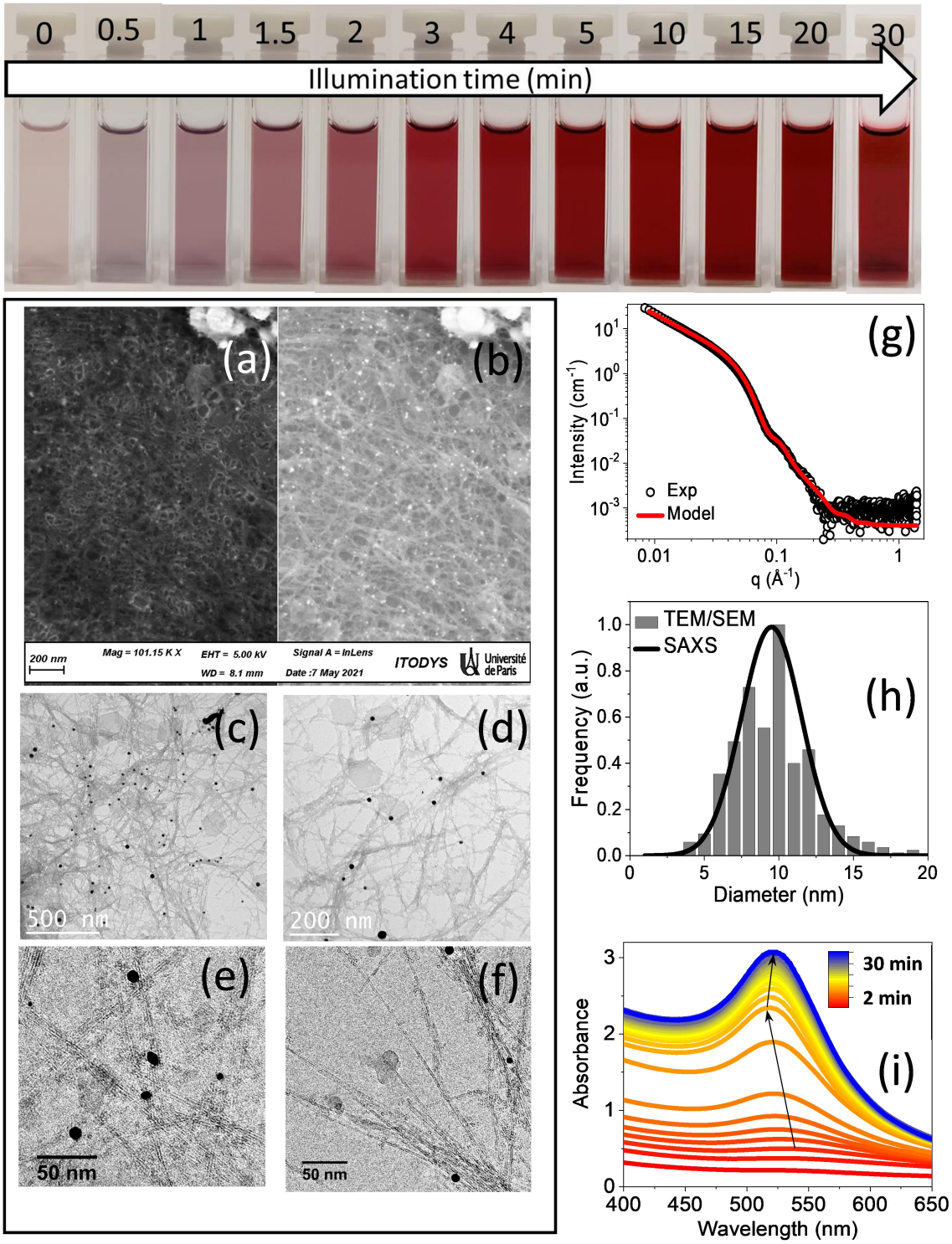

Figure 2. *Photographs of the aqueous gold-containing Imo-CH_3 solution (Solution-A) at different illumination times during UV photolysis (top). Images of gold nanoparticles attached to Imo-CH_3 nanotubes by SEM (a,b), conventional TEM (c,d) and cryo-TEM (e,f); SAXS profile (circles) of photolytically-produced GNP-coupled Imo-CH_3 NTs after subtraction of the pristine Imo-CH_3 scattering contribution and its simulated SAXS profile (red line) (g), size distribution histogram of gold nanoparticles (h) and evolution of UV-Vis absorption spectra during photolysis of Solution-A (without further dilution)(i).*

3.2.2. Gamma-radiolysis of Solution-A

Solution-A turned from light pink to a red color characteristic of GNPs during gamma irradiation in the presence of propan-2-ol (10% per volume) (Figure 3, top). Figure 3a and Figure 3b,c show the conventional SEM and TEM images of the sample, respectively. Cryo-TEM images provided in Figure 3d show spherical GNPs deposited on Imo-CH_3 by radiolytic reduction. As after photolysis, the radiolytically-produced nanoparticles are attached to the external surface of the Imo-CH_3 NTs. The SAXS profile of the radiolytically-formed GNPs on Imo-CH_3 also indicates the formation of spherical GNPs with a diameter of 5 ± 2 nm (see Figure 3f and Table S4 in the Electronic Supplementary Information for the parameters extracted from the SAXS analysis). The size distributions extracted from SEM/TEM and SAXS analysis are shown in Figure 3e. Clearly, the radiolytically-synthesized nanoparticles (~5 nm) are smaller than those synthesized by photolysis (~9.5 nm). Figure 3g shows the evolution of UV-Vis absorption spectra of *Solution-A* at various irradiation doses (expressed in Gy) during gamma radiolysis. The increased intensity of the absorption maximum around 530 nm also confirms the formation of plasmonic GNPs under gamma radiolysis (Figure 3h).

The gold volume fraction (3.2×10^{-6}) calculated from the number density of particles (SAXS data) and average volume per particle (SAXS data) is smaller than that expected from the total gold composition (9.8×10^{-6}) obtained by ICP-MS. Indeed, these latter measurements lead to a value of 8.2 ± 0.1 % w/w of gold attached to Imo-CH_3 NTs, which is consistent with the

targeted concentration of 8.5 wt%. As in the sample synthesized after photolysis, the missing gold atoms ($67\%_{v/v}$) can be the result of the presence of smaller clusters, whose signal is hidden by the imogolite contribution at high scattering vector.

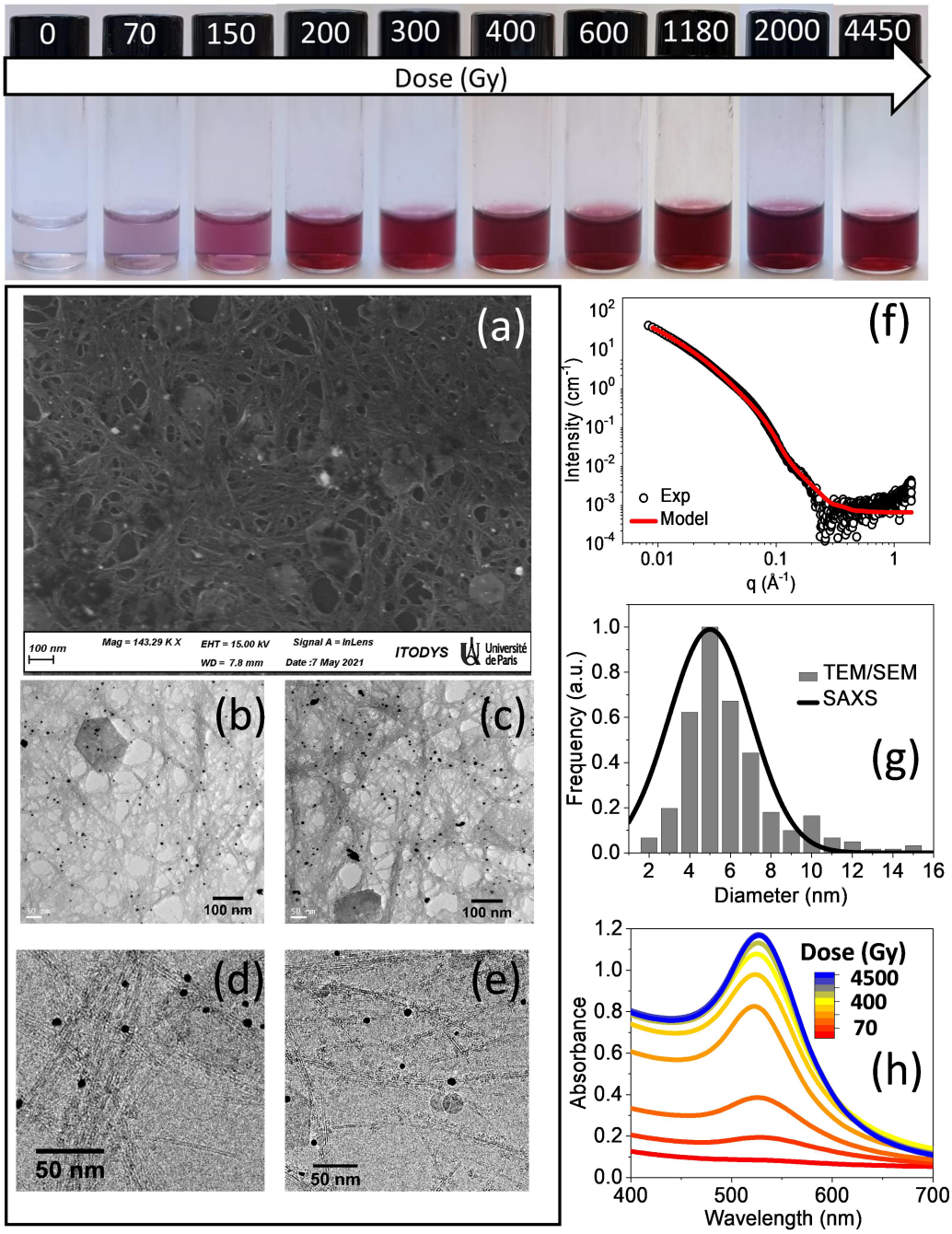

Figure 3. *Photographs of GNPs-Imo-CH_3 aqueous Solution-A at different irradiation doses (top) during gamma radiolysis of Solution-A. Images of GNPs attached to Imo-CH_3 nanotubes by SEM (a), conventional TEM (b,c) and cryo-TEM (d,e); SAXS profile of the radiolytically-produced GNPs-decorated Imo-CH_3 NTs subtracted with pristine Imo-CH_3 scattering contribution and simulated SAXS profile (f), size distribution histogram of GNPs (g), evolution of UV-Vis absorption spectra during gamma radiolysis of Solution-A (diluted 3 times with millipore water prior to the UV-Vis spectroscopy measurements)(h).*

For both photolysis and gamma-radiolysis of *Solution-A*, the integrity (stability) of imogolite nanotubes was checked by FT-IR spectroscopy. FT-IR study confirmed that the tubular morphology of Imo-CH_3 remains intact after coupling with GNPs by photolytic/radiolytic reduction (see Section 8 in Electronic Supplementary Information).

3.3. X-ray Photoelectron Spectroscopy (XPS) of GNP-coupled Imo-CH_3

The XPS survey spectra of GNP-coupled Imo-CH_3 NTs, prepared by UV photolysis and gamma radiolysis of Solution-A, are shown in Figures 4a and 4c, respectively. The peaks corresponding to Al 2p, Si 2p, C 1s, O 1s, Cl 2p and Au 4f were detected. The first four contributions mainly arise from Imo-CH_3 NTs, whereas the latter two arise from Cl^- ions and GNPs attached to the Imo-CH_3 surface. High-resolution Au 4f XPS core-level spectra are shown in Figures 4b and 4d for GNP-coupled Imo-CH_3 NTs prepared by UV photolysis and gamma radiolysis, respectively. The characteristic metallic doublet of Au 4f is clearly seen on the spectra. The curve fitting of the Au 4f core-level spectrum was performed using two spin-orbit split $4f_{7/2}$ and $4f_{5/2}$ components, separated by about 3.7 eV in an intensity ratio $4f_{7/2}$: $4f_{5/2}$= 4:3. The binding energy of the $4f_{7/2}$ spin-orbit component was equal to 84.4 and 84.1 eV for samples after photolysis and radiolysis, respectively. The binding energies of both spin-orbit components were slightly shifted towards higher values as compared to macroscopic gold (Au $4f_{7/2}$= 84.0 eV in this latter case),[46] which is

in agreement with the XPS measurement of nanometric gold by Peters *et al.*[47] The appearance of characteristic metallic doublets in the Au 4f core-level spectra of both the photolytically and radiolytically reduced systems further suggests that the majority of gold exists as metallic gold nanoparticles (Figures 4b and 4d). However, unlike the radiolytically-synthesized nanoparticles (Figure 4d), in the case of the photolytically-synthesized GNPs (Figure 4b), another doublet, shifted by ~ 1.4 eV to the higher binding energy, is also observed. This additional doublet may be attributed to the presence of gold oxide species (or to non-reduced species). The small binding energy shift of 1.4 eV could be due to the formation of oxidized Au^{+I} species, possibly in the form of AuO^- species on the Imo-CH_3 surface.[48-50] In general, gold oxides, as Au_2O_3, the most common gold oxide species present at the macroscopic scale, are known to exhibit limited stability and to decompose readily upon low heat treatment or irradiation.[51] The higher stability of oxides detected in the sample having undergone reduction through photolysis, may be related to the origin of the electrons. Indeed, in this case, the reducing electrons are mainly coming from the nanotube surface. This may favor the close interaction between reduced gold atom and the surface oxygen atoms. The estimation of the oxide-to-metal 4f peak area ratio gives a rough approximation of around 20 at% of gold existing as an oxide, and thus closely attached to the AlO surface. On the contrary, for the radiolytic synthesis of GNPs, reducing species mainly came from the solution. In this case, the nanoparticles formed are then pure gold metal nanoparticles, as proven by the absence of the oxide doublet in the Au 4f core-level spectra (Figure 4d).

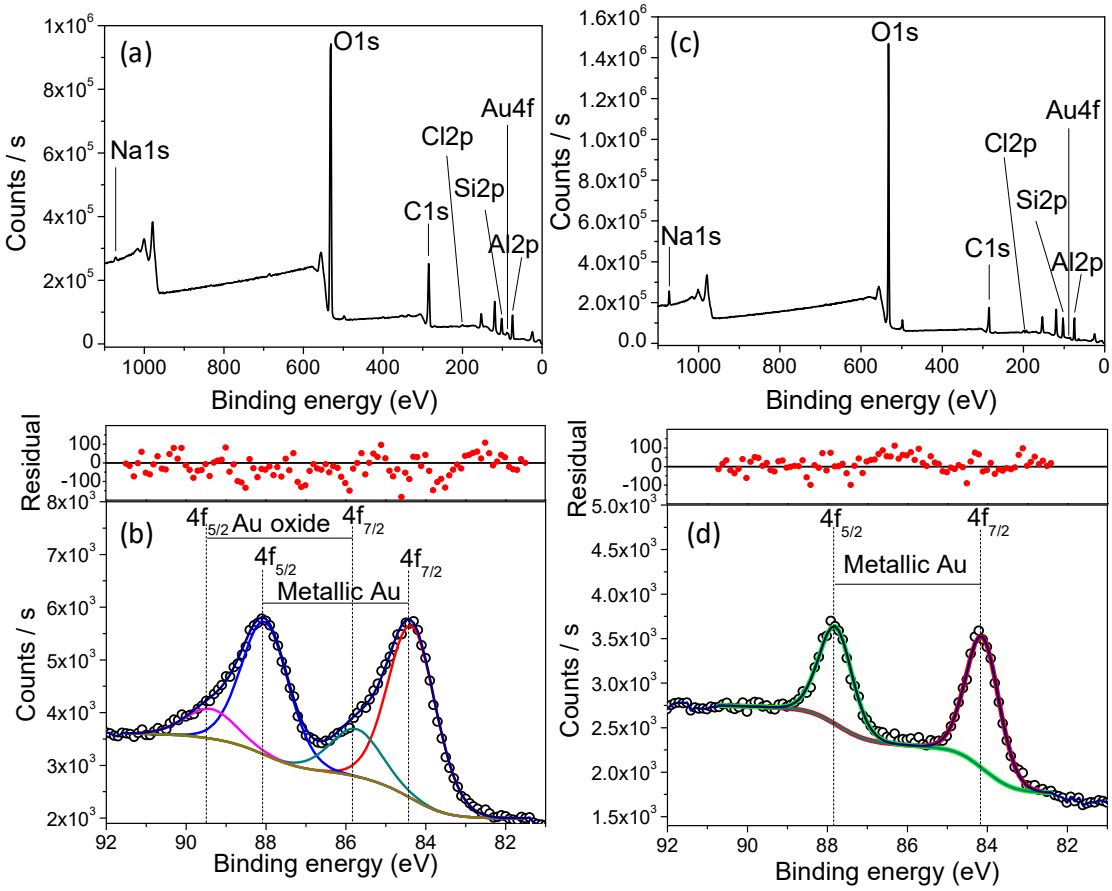

Figure 4. *XPS survey and Au 4f photoelectron core-level spectra of GNPs attached to Imo-CH_3 NTs prepared by UV photolysis (a,b) and gamma radiolysis (c,d).*

3.4. Reactivity of Imo-CH_3 NTs as photoreactors

3.4.1. Bare Imo-CH_3 under UV illumination

Figure 5a presents the yields of gases produced upon UV illumination (at 254 nm, corresponding to 4.9 eV) of an aqueous solution of pristine Imo-CH_3. We observed that a low amount of gas is produced (see Table 1). Indeed, the band gap of Imo-CH_3 was measured as 5.4 eV.[19] Therefore, only a very small fraction of the incident light enables its direct photo-excitation. However, due to the wall polarization of Imo-CH_3, which was estimated to be around 0.2 eV,[19] charge

separation is expected to be favored, which, in turn, enhances reactivity. The energy of the electron/hole pair produced by direct excitation of Imo-CH_3 has been measured recently.[19] The directly photo-excited electrons can reach a potential of -1.45 V (vs. NHE) (conduction band energy), making them potentially highly reducing species. At the same time, the hole has a potential of ~4 V (vs. NHE), allowing oxidation of many encapsulated molecules.

The redox balance of the produced gases in the case of bare imogolite is very interesting. CO_2, CO, CH_4 and H_2 were detected and quantified (Table 1). Noteworthily, as Imo-CH_3 NTs were shown to be extremely stable under UV illumination for 5 hours, the possibility of photo-degradation of internal methyl groups in Imo-CH_3 NTs could be ruled out.[21] In the present work, propan-2-ol was used as a sacrificial electron donor (hole scavenger) to ultimately produce carbon dioxide (CO_2). The only carbon source being then propan-2-ol, it is reasonable to assume that the carbonaceous gases arise from the oxidation of propan-2-ol inside the Imo-CH_3 cavity thanks to the strong oxidizing power of photo-exited holes. The source of oxygen atoms can be attributed to both propan 2-ol and water molecules. Indeed, infrared experiments have shown that water vapor can penetrate into the hydrophobic cavity of Imo-CH_3.[52] Moreover, the contribution of hydroxyl radicals arising from the oxidation of water and leading to the production of carbon dioxide was already proven by our group in the case of the degradation of DBAN in a UV-illuminated Imo-CH_3 suspension.[21]

The global reactions, leading to the formation of CO_2, but also of CH_4, are written below:

$$C_3H_7OH + 18\ h^+ + 5\ H_2O \rightarrow 3\ CO_2 + 18\ H^+ \qquad (R1)$$

$$C_3H_7OH + 10\ h^+ + 3\ H_2O \rightarrow 2\ CO_2 + CH_4 + 10\ H^+ \qquad (R2)$$

According to (R1) and (R2), each CO_2 molecule produced by the internal oxidation of propan-2-ol will require between 5 and 6 photo-excited holes.

The initial production rate of the various gases per gram and per illumination hour is given in Table 1 for pristine Imo-CH_3 and the evolution of gas production yield with irradiation time can be seen in Figure 5a. The initial rates should give a better idea of the early processes. Hereafter, we will assume that the active photo-generated holes can only be involved in reaction R1 and R2 with respective probabilities of p and 1-p. This assumption is based on the efficient confinement within Imo-CH_3 NTs, which favors complete mineralization of reaction products as has already been observed for DBAN.[20] Electrons are responsible for the production of H_2 from the reduction of H^+ (two electrons per molecule) and CO from CO_2 (two electrons per molecule). CH_4 can be produced directly by (R2) and also by reduction of CO_2 (8 electrons per molecule). If we assume p = 1 (only (R1) pathway), then CO and CH_4 can only be produced from the reduction of CO_2. Therefore, a total of 16.1 $\mu mol.g^{-1}.h^{-1}$ of CO_2 has to be initially produced by the oxidation of propan-2-ol (CO_2 + CO + CH_4 production from Table 1). This requires 96.6 $\mu mol.g^{-1}.h^{-1}$ of photo-exited holes involved in chemical oxidation reactions. On the reduction side, 16.3 $\mu mol.g^{-1}.h^{-1}$ of H_2 is produced, which requires 32.6 $\mu mol.g^{-1}.h^{-1}$ of photo-exited electrons. Moreover, there are also 4.2 $\mu mol.g^{-1}.h^{-1}$ of CH_4 (corresponding to 33.6 $\mu mol.g^{-1}.h^{-1}$ required e^-) and 2.6 $\mu mol.g^{-1}.h^{-1}$ of CO (5.2 $\mu mol.g^{-1}.h^{-1}$ required e^-). Therefore, roughly 71 $\mu mol.g^{-1}.h^{-1}$ electrons are required to account for all the considered reduction reactions, a lower value than that estimated for photo-excited holes. This means that some of the electrons were involved in other reduction reactions leading to products that were not measured. This can be either the reduction of trace residual dioxygen or the trapping of photo-exited electrons in Imo-CH_3 defects as previously described in the literature.[53] If we consider all reactions, the minimum possible

value of *p* is equal to 0.3 (see Section 9 of the Supporting Information for more details). This value corresponds to the case where r1 = 0 (see Section 9 of the Supporting Information to know about r1) and all the observed CH_4 has been produced by the (R2) pathway. In this case, a total of ~62 $\mu mol.g^{-1}.h^{-1}$of photo-exited holes are required (see Figure S7 of the Supporting Information). In the reduction case, only 37.8 $\mu mol.g^{-1}.h^{-1}$ of photo-exited electrons are involved in the reduction of H^+ and CO_2 to give H_2 and CO, respectively. In this case again, a significant number of the electrons are involved in other reduction reactions. Once again, the reduction of residual dioxygen or the trapping of electrons in Imo-CH_3 defects could be invoked. Thus, part of the electrons involved in the reduction of residual dioxygen could lead to the formation of hydrogen peroxide. The consumption of residual dioxygen and the production of H_2O_2 could also explain the increase in the rates of gas production with each irradiation hour as observed for pristine Imo-CH_3 NTs.

3.4.2. GNP-coupled Imo-CH_3 under UV illumination

As discussed before, the UV illumination of a semiconductor photocatalyst involves band gap excitation of the semiconductor and migration of electron/hole pairs to the surface, thereby using them to perform reduction and oxidation reactions on the photocatalyst surface. In a semiconductor photocatalyst coupled with a noble metal co-catalyst, the course of the reduction reaction is driven by the ease of electron transport from the light harvesting semiconductor to the noble metal (trapping of electrons by the co-catalyst). The probability of electron transport is largely influenced by the work function of the noble metal co-catalyst. In the coupled system, both Imo-CH_3 and GNPs can absorb UV light, and the quality of the Imo-CH_3/GNP junction is very important for the behavior of photo-generated charges. Gold has a bulk work function of 5.1 eV. Although this value can decrease with the size of GNPs, 5-10 nm GNPs should still have a

work function of around 3.6 eV, corresponding to a potential of the Fermi level of -0.9 V vs. NHE.[54] Therefore, the energy of the bottom of the conduction band of Imo-CH_3 (-1.45 V vs. NHE) is high enough to allow the transfer of photo-exited electrons to the GNPs and facilitates charge separation due to the formation of a Schottky barrier[31] at the Imo-CH_3/GNP interface. The photoluminescence measurements corroborate this hypothesis. Figure S7 (Electronic Supplementary Information) shows the fluorescence emission spectra of Imo-CH_3 NTs in aqueous solution at different excitation wavelengths. Two emission peaks of different intensity are obtained at 366 nm (3.5 eV) and 580 nm (2.1 eV) after an excitation at 220 nm (5.6 eV) (Figure S7c). Figure S8 (Electronic Supplementary Information) shows the fluorescence emission spectra of pristine Imo-CH_3 after excitation at 220 nm compared to Imo-CH_3 coupled with GNPs prepared by both UV photolysis and gamma radiolysis. The emission intensities are normalized with respect to the absorbance at 220 nm. Clearly, the energy loss by radiative decay is strongly reduced in presence of GNPs. It is also interesting to note that the ratio between the 366 nm and 588 nm peaks is nearly the same for bare and photolytic GNP-coupled NTs while it is changed for the radiolytic GNP-coupled NTs. The photolytic and radiolytic couplings thus have a different impact on the nanotubes' energy levels. These results also suggest that the photo-generated electrons are effectively guided toward the GNPs. In addition to the facilitated charge separation in presence of GNPs as co-catalysts (change of electronic properties), the catalytic properties of GNPs are also important in driving the photocatalytic processes. As far as the photocatalytic H_2 production on Imo-CH_3/GNP coupled system is concerned, the combination of surface H atoms (formed by photocatalytic reduction of H^+) into molecular H_2 is also an important parameter in deciding the rate of the photocatalytic process, which largely depends on the Au-H bond strength. Gold, being on the top side of the Trassatti's volcano curve[55] (showing the relation between the metal-H bond strength and the exchange current for H_2 evolution), demands less energy for

evolution into molecular H_2. Thus, considering both the electronic effect and the catalytic effect, GNPs acted as a suitable co-catalyst in the present work.

Concerning the initial gas production rates upon UV illumination (see Table 1 with the various amounts of gases per mass and illumination time units), the most striking difference between GNP-coupled Imo-CH_3 and the pristine sample was the significant increase in H_2 production. Indeed, its production per mass and illumination time unit was multiplied by a factor of roughly 90 and 10 in the samples obtained after photolysis and radiolysis, respectively, as compared to the pristine NTs. We also observed a change in the rate of production of C1 gases (CO_2, CO, CH_4), but they did not follow the same trend for the photolytically and radiolytically prepared samples. Therefore, the redox balance based on the measured gases is far from being equilibrated. Indeed, in this case, a vast majority of oxidized species is missing.

If we assume that GNP coupling does not change the effective confinement of oxidation products inside Imo-CH_3 NTs, then, the production of C1 carbonaceous gases is still a metric of the confined oxidation activity. For radiolytic GNP-coupled NTs, the total amount of C1 gas produced increased from 16.1 in Imo-CH_3 to 31.9 $\mu mol.g^{-1}.h^{-1}$ in the gold-coupled sample, i.e., it increased by a factor of roughly 2. Therefore, the coupling with the GNPs produces an enhancement of the oxidation activity inside the NTs. The total electron amount consumed to explain the produced gases (H_2, CO and CH_4) is 444.8 $\mu mol.g^{-1}.h^{-1}$. Based on the photo-excited holes required to produce the 31.9 $\mu mol.g^{-1}.h^{-1}$ of CO_2 (corresponding to CO_2 + CO + CH_4 production as explained above) inside the NTs by the (R1) pathway (191.4 $\mu mol.g^{-1}.h^{-1}$), only ~43% of the electrons involved in reduction reactions would correspond to photo-electrons produced by direct photo-excitation of the NTs. This means that the enhancement comes from a

direct UV excitation of the GNPs or of the gold molecular clusters and that 57% of the hole scavenging activity probably occurs outside the NTs, producing oxidized species like acetone.

For photolytic GNPs coupled to Imo-CH_3 NTs, the enhancement factor of C1 gas production is even stronger. A total of 118.3 $\mu mol.g^{-1}.h^{-1}$ CO_2 molecules were produced (corresponding to CO_2 + CO + CH_4 production as explained above), which represents ~7 times more than for the bare Imo-CH_3 sample. On one hand, between 710 $\mu mol.g^{-1}.h^{-1}$ (considering (R1)) and 592 $\mu mol.g^{-1}.h^{-1}$ (considering (R2)) of photo-excited holes are required to explain the formation of all these C1 gases. On the other hand, for (R1), the production of H_2, CO and CH_4 requires a total of 3480 $\mu mol.g^{-1}.h^{-1}$ photo-exited electrons. In this case, considering reaction (R1), 20% of the photo-catalytic activity takes place in the NTs and 80% of the hole scavenging activity probably occurs outside the nanotubes. In such a case, because no confinement effects are active, the hole scavenging by propan-2-ol directly on GNP catalyst leads to the production of acetone and of ethanal, as evidenced by GC-MS experiments (see Figure S9, Electronic Supplementary Information). These molecules can diffuse freely away from the GNPs surface.[56] The fact that the GNP coupling enables a significant enhancement of the internal oxidative reactivity tends to show that the limiting factor of the efficiency of pristine Imo-CH_3 is probably the dihydrogen evolution reaction on the external surface.

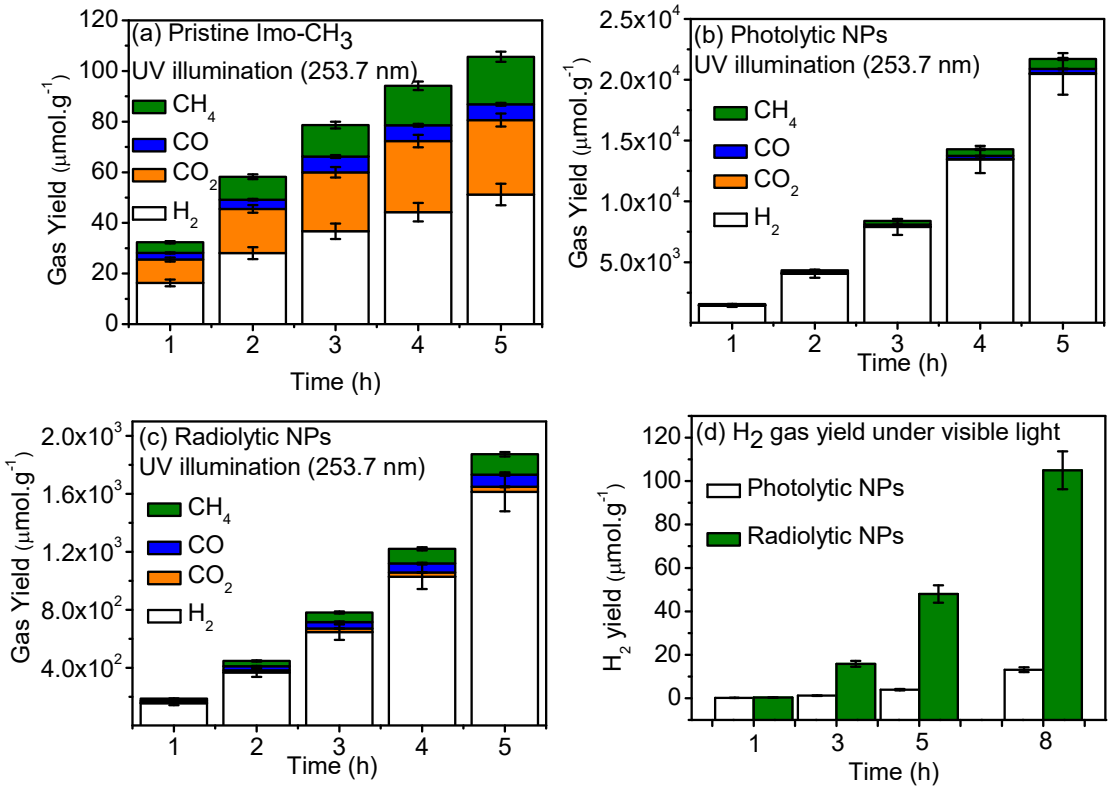

Figure 5.*Gases produced as a function of UV illumination time for aqueous solutions of pristine (a) and GNP-coupled Imo-CH_3 NTs prepared by photolytic (b) and radiolytic (c) routes. H_2 yield produced during visible light illumination of aqueous solutions of GNP-coupled Imo-CH_3 NTs (d).*

Table 1. *Initial rates of gases produced for bare and GNP-coupled Imo-CH_3 NTs under UV light illumination.*

Gases produced	**Amount of gases produced under UV light (254 nm) ($\mu mol.g^{-1}.h^{-1}$)**		
	Imo-CH_3	**Photolytic NPs**	**Radiolytic NPs**
H_2	16.3 ± 1.3	1443 ± 120	155 ± 12.9
CO_2	9.3 ± 0.8	19.2 ± 1.7	7.7 ± 0.7
CO	2.6 ± 0.2	33.1 ± 2.9	9.8 ± 0.9
CH_4	4.2 ± 0.4	66.0 ± 7.0	14.4 ± 1.5

3.4.3. Difference in the photocatalytic activity of nanomaterials obtained by UV photolyis and gamma-radiolysis

The observed difference in photocatalytic activity between the GNP-Imogolite photocatalysts prepared by UV photolysis and gamma radiolysis seems to depend on the chemical property of the GNPs and their attachment with the Imo-CH_3 walls. It is important to note that the nature of the contacts between the GNPs and the Imo-CH_3 surface is not the same for photolytically- and radiolytically- synthesized systems. As confirmed by XPS study, stable nanoscale gold metal/oxide species are formed on the Imo-CH_3 surface by UV photolysis, consisting of around 20% gold in partially oxidized or non-reduced form. This is because, during the photolytic synthesis, apart from the possible direct reduction of gold precursors under UV light by self-excitation or by some photolytically generated intermediates (reducing molecules or radicals), photo-deposition of gold atoms on the Imo-CH_3 surface is one of the major mechanisms for GNPs growth, where the reducing electrons originate from the external surface of Imo-CH_3 NTs due to its own excitation under UV light. This favors a stronger coupling between the Imo-CH_3 NTs and the attached GNPs produced photolytically, which may result in a better energy level alignment and thus a better charge separation (transfer of electrons from Imo-CH_3 to GNPs). This explains the stronger improvement of the C1 gas production (×7) under UV illumination in Imo-CH_3 coupled to photolytic GNPs. On the contrary, gamma radiolysis produced pure metallic GNPs on the Imo-CH_3 surface (as seen from XPS), where the reduction of gold precursors majorly took place by the solvated electrons and the reducing radicals originated from the excitation of the solvent. Thus, the interaction between the radiolytically formed GNPs and the Imo-CH_3 surface is expected to be of Van der Waals type, resulted in a weaker coupling compared to the photolytically-produced sample. This resulted in less efficient charge separation

and thus lower photocatalytic activity of the radiolytically produced system under UV light (increases the photocatalytic oxidation activity of the nanotube only by a factor of ~2). Moreover, in the case of the water-gas shift reaction that converts CO and H_2O to H_2 and CO_2, Flytzani-Stephanopoulos *et al.* have shown the important role of Au-oxide species instead of GNPs as active sites of gold supported on oxide materials.[48,57] The presence of these gold oxide species in the case of the GNPs formed after photolysis, may also favor gas production in these samples. Note that the precise location of the reduction and oxidation reactions due to gold is still an open question, as the samples contain a large fraction of small gold clusters, which are known to be highly reactive.58,[59] Lastly, it is worth pointing out that the results obtained with the photolytic coupling of GNPs represent very encouraging H_2 production rates. This is all the more interesting since in the full UV flux of 4.8 eV average energy, only a small fraction has energy higher than the Imo-CH_3 band gap value. The visible light also proved efficient in generating photocatalytic activity (see Figure 5d). In this case, the reactivity comes from the relaxation of the GNP surface plasmons. This aspect should be explored further. A deeper mechanistic investigation of the charge carrier dynamics at the GNP-Imogolite interface is required to better understand the observed difference in photocatalytic activity. However, such a detailed study was beyond the scope of the present work.

4. Conclusions

Surfaces of methyl imogolite (Imo-CH_3) nanotubes were functionalized with uncapped gold nanoparticles (GNPs) by deposition-precipitation followed by UV photolysis or gamma-radiolysis. The comparison of different measurements revealed a missing volume fraction of gold in both the photolytically and radiolytically prepared samples. This suggested that a significant

fraction of gold existed on the Imo-CH_3 surface as Au(0) atoms or ultrasmall clusters (< 1 nm) that could not be detected by either SAXS or by electron microscopy techniques.

The photocatalytic activity of bare Imo-CH_3 NTs evidenced a strong confinement effect of the oxidation part (inside), with reduction reactions occurring on the external surface of the NTs. Establishing a redox balance revealed that some reduced species were not identified. Imo-CH_3 NTs coupled with GNPs having an average size of 5 nm and a full metallic character (radiolytically-produced GNPs) exhibited a global ~10 times more H_2 production than bare Imo-CH_3. Imo-CH_3 coupled with GNPs having an average particle size of 10 nm with partially oxidized gold species (photolytically-produced GNPs) showed a ~90-times enhancement of H_2 production compared to bare Imo-CH_3. The direct photocatalytic activity of Imo-CH_3 represented only 20% of the total reactivity, and in this sample most of the photocatalytic behavior was indeed due to the gold surface. This study paves the way for the optimization of gold nanoparticles attached to imogolite nanotubes as photocatalytic nano-reactors. This system appears to be, thus, very promising as a competitive photocatalytic nano-reactor, which could benefit from multiple synergies due to confinement, polarization and band engineering.

Conflicts of interest: There are no conflicts of interest to declare.

Acknowledgments: The ANR BENALOR (grant number ANR-20-CE09-0029), the DIM RESPORE (GRANITE project, 2019-2020) and the CEA (PHOTOTUBE project, Bottom Up 2020-21) are thoroughly acknowledged for their financial support for the post-doctoral grant of Dr. S. Patra. The project proposal GRANITE, submitted jointly by Dr. S. Patra and Dr. A. Thill, received the Marie Sklodowska Curie Actions Seal of Excellence (SoE) award from the European Commission for the MSCA-IF-2018 call. The authors thank Dr. Mark A. Levenstein for reading

the manuscript and many insightful comments. Dr. S.G. Derrouich and Dr. P. Decorse are also acknowledged for SEM and XPS characterizations, respectively. XPS equipment was funded by the Région Île-de-France, convention SESAME n°16016303 and the Labex SEAM (Science and Engineering for Advanced Materials and devices).

References

1. X. Liu, J. Iocozzia, Y. Wang, X. Cui, Y. Chen, S. Zhao, Zhen Li, Z. Lin, *Energy Environ. Sci.,* 2017, **10**, 402-434.
2. R. Jiang, B. Li, C. Fang, J. Wang, *Adv. Mater.*, 2014, **26**, 5274-5309.
3. P. Rai, *Sustainable Energy Fuels,* 2019, **3**, 63-91.
4. U. Banin, Y. Ben-Shahar, K. Vinokurov, *Chem. Mater.,* 2014, **26**, 97-110.
5. N. Waiskopf, Y. Ben-Shahar, U. Banin, *Adv. Mater.,* 2018, **30**, 1706697 (1-10).
6. R. Jiang, B. Li, C. Fang, J. Wang, *Adv. Mater.,* 2014, **26**, 5274-5309.
7. J. Yu, Q. Xiang, M. Zhou, *Applied Catalysis B: Environmental* 2009, **90**, 595-602.
8. J. Yu, M. Jaroniec, *Phys. Chem. Chem. Phys.,* 2011,**13**, 4853-4861.
9. H.G. Yang, C.H. Sun, S.Z. Qiao, J. Zou, G. Liu, S.C. Smith, H.M. Cheng, G.Q. Lu, *Nature* 2008, **453**, 638-642.
10. S. Liu, J. Yu, M. Jaroniec, *J. Am. Chem. Soc.,* 2010, **132**, 11914-11916.
11. Y. Liu, Y-X. Yu, W-D. Zhang, *J. Phys. Chem. C* 2013, **117**, 12949-12957.
12. K. Woan, G. Pyrgiotakis, W. Sigmund, *Adv. Mater.,* 2009, **21**, 2233-2239.
13. I. Bottero, B. Bonelli, S. E. Ashbrook, P. A. Wright, W. Zhou, M. Tagliabue, M. Armandi and E. Garrone, *Phys. Chem. Chem. Phys.,* 2011, **13**, 744-750.

14. E. Poli, J.D. Elliott, L.E. Ratcliff, L. Andrinopoulos, J.Dziedzic, N.D.M. Hine, A.A. Mostofi, C.-K. Skylaris, P.D. Haynes, G. Teobaldi, *J. Phys.: Condens. Matter,* 2016, **28**, 074003.
15. J.D. Elliott, E. Poli, I. Scivetti, L.E. Ratcliff, L. Andrinopoulos, J. Dziedzic, N.D.M. Hine, A.A. Mostofi, C.-K. Skylaris, P.D. Haynes, G. Teobaldi, *Adv. Sci.,* 2017, **4**, 1600153.
16. E. Poli, J. D. Elliott, S. K. Chulkov, M. B. Watkins and G. Teobaldi, *Front. Chem.,* 2019, **7**, 210.
17. G. Monet, M. S. Amara, S. Rouzière, E. Paineau, Z. Chai, J. D. Elliott, E. Poli, L.-M. Liu, G. Teobaldi and P. Launois, *Nat. Commun.,* 2018, **9**, 2033.
18. P. Picot, F.Gobeaux, T.Coradin, A.Thill, Dual internal functionalization of imogolite nanotubes as evidenced by optical properties of Nile red, *Applied Clay Science* 2019, **178**, 105133.
19. M-C. Pignie, V. Shcherbakov, T. Charpentier, M. Moskura, C. Carteret, S. A. Denisov, M. Mostafavi, A. Thill, S. Le Caër, *Nanoscale,* 2021, **13**, 3092.
20. M-C. Pignie, S. Patra, L. Huart, A. Milosavljevic, J-P. Renault, J. Leroy, C. Nicolas, O. Sublemontier, S. Le Caer, A. Thill, *Nanoscale,* 2021, **13**, 19650-19662.
21. S. Patra, D. Schaming, P. Picot, M-C. Pignié, J-B. Brubach, L. Sicard, S. Le Caër, A. Thill, *Environ. Sci.: Nano,* 2021, **8**, 2523-2541.
22. N. Wu, *Nanoscale,* 2018, **10**, 2679-2696.
23. S.K. Cushing, N. Wu, *J. Phys. Chem. Lett.* 2016, **7**, 666-675.
24. W. Hou, S.B. Cronin, Adv. Funct. Mater.,2013, **23**, 1612-1619.
25. S. Linic, P. Christopher, D.B. Ingram, *Nat. Mater.,*2011, **10**, 911-921.
26. T. Hirakawa, P.V. Kamat, *J. Am. Chem. Soc.,* 2005, **127**, 3928-3934.

27. Z.W. Seh, S. Liu, M. Low, S-Y. Zhang, Z. Liu, A. Mlayah, M-Y. Han, *Adv. Mater.,* 2012, **24**, 2310-2314.

28. A.L. Lunaa, F. Mattera, M. Schrecka, J. Wohlwenda, E. Tervoorta, C. Colbeau-Justinb, M. Niederbergera, *Applied Catalysis B: Environmental* 2020, **267**, 118660 (1-10).

29. S. Atta, A.M. Pennington, F.E. Celik, L. Fabris, *Chem* 2018, **4**, 2140-2153.

30. L. Qin, G. Wang, Y. Tan, *Scientific Reports* 2018, **8**, 16198 (1-13).

31. J. Yang, D. Wang, H. Han, C. Li, Roles of cocatalysts in photocatalysis and photoelectrocatalysis, *Acc. Chem. Res.* 2013, **46**, 8, 1900–1909.

32. L.M. Liz Marzan, A.P. Philipse, *Colloids and Surfaces A: Physicochemical and Engineering Aspects* 1994, **90**, 95-109.

33. L.M. Liz-Marzan, A.P. Philipse, *J. Phys. Chem.* 1995, **99**, 15120-15128.

34. J.R. Boltona, M.I. Stefanb, P.-S. Shawc, K.R. Lykkec, *J. Photochem. Photobiol. A,* 2011, **222**, 166-169.

35. H. Fricke, E.J. Hart, in Radiation Dosimetry (eds F.H. Attix and W.C. Roesch,) Vol. 2, 167-232, Academic, 1966.

36. CEA-IRAMIS-LIONS, Python for Small Angle X-ray Scattering data acquisition, treatment and computation of model SAXS intensities. https://pypi.org/project /pySAXS/.

37. O. Taché, S. Rouzière, P. Joly, M. Amara, B. Fleury, A. Thill, P. Launois, O. Spalla, B. Abécassis, *J. Appl.Crystallogr.,* 2016, **49**, 1624-1631.

38. M.P. Casaletto, A. Longo, A. Martorana, A. Prestianni, A.M. Venezia, *Surface and Interface Analysis,* 2006, **38**, 215-218.

39. P. Picot, Nanotube inorganique d'imogolite à cavité interne hydrophobe: synthèse, fonctionnalisation et encapsulation de molécules organiques,PhDthesis, Université Paris-Saclay 2019, http://www.theses.fr/2019SACLS051.

40. J.B. Harsh, S.J. Traina, J. Boyle, Y. Yang, *Clays and Clay Minerals,* 1992, **40**, 700-706.

41. C. Su, J.B. Harsh, *Clays and Clay Minerals,* 1993, **41**, 461-471.

42. J.P. Gustafsson, *Clays and Clay Minerals,* 2001, **49**, 73-80.

43. S. Tsubota, D.A.H. Cunningham, Y. Bando, M. Haruta, *Stud. Surf. Sci. Catal.,* 1995, **91**, 227-235.

44. M. Haruta, *Catalysis Surveys from Asia,*1997, **1**, 61-73.

45. C. Su, J.B. Harsh, *Clays and Clay Minerals,* 1993, **41**, 461-471.

46. M. Tchaplyguine, M-H. Mikkelä, C. Zhang, T. Andersson, O. Björneholm, *J. Phys. Chem. C,* 2015, **119**, 8937-8943.

47. S. Peters, S. Peredkova, M. Neeb, W. Eberhardt, M. Al-Hada, *Surface Science,* 2013, **608**, 129-134.

48. Q. Fu, H. Saltsburg, M. Flytzani-Stephanopoulos, *Science* 2003, **301**, 935-938.

49. M.P. Casaletto, A. Longo, A. Martorana, A. Prestianni, A.M. Venezia, *Surf. Interface Anal.,*2006, **38**, 215-218.

50. J.J. Pireaux, M. Liehr, P.A. Thiry, J.P. Delrue, R. Caudano, *Surf.Sci.,* 1984, **141**, 221-232.

51. B. Koslowski, H.-G. Boyen, C. Wilderotter, G. Kästle, P. Ziemann, R. Wharenberg, P. Oelhafen, *Surf.Sci.,* 2001, **475**, 1-10.

52. Y. Liao, P. Picot, M. Lainé, J-B. Brubach, P. Roy, A. Thill, S. Le Caër, *Nano Research,* 2018, **11**, 4759-4773.

53. M. Hureau, A. Moissette, A. Legrand, F. Luchez, M. Sliwa, C. Bremard, *J. Phys. Chem. C,* 2012, **116**, 9092-9105.

54. Y. Zhang, O. Pluchery, L. Caillard, A-F. Lamic-Humblot, S. Casale, Y.J. Chabal, M. Salmeron, *Nano Lett.,* 2015, **15**, 51-55.

55. S. Trasatti, Work function, electronegativity, and electrochemical behaviour of metals: III. Electrolytic hydrogen evolution in acid solutions, J. Electroanal. Chem. 1972, **39**, 163-184.

56. V. Shcherbakov, S.A. Denisov, M. Mostafavi, *Phys. Chem. Chem. Phys.,* 2021, **23**, 26494-26500.

57. M. Flytzani-Stephanopoulos, *Acc. Chem. Res.,* 2014, **47**, 783-792.

58. B. Weng, K.Q. Lu, Z. Tang, H.M. Chen, Y.J. Xu, *Nat.Commun.,* 2018, **9**, 1-11.

59. K. Katsiev, G. Harrison, Y. Al-Salik, G. Thornton, H. Idriss, *ACS Catalysis,* 2019, **9**, 8294-8305.